

1
2
3
4
5
6
7
8
9
10
11
12
13
14
15
16
17
18
19
20
21
22
23
24
25

UNIVERSITY OF CALIFORNIA
SANTA CRUZ

**AN INCLUSIVE SEARCH FOR THE DECAY OF A BOOSTED
HIGGS BOSON IN THE $H \rightarrow b\bar{b}$ CHANNEL WITH THE ATLAS
DETECTOR**

A dissertation submitted in partial satisfaction of the
requirements for the degree of
DOCTOR OF PHILOSOPHY

in

PARTICLE PHYSICS

by

Jacob Martin Pasner

October 2019

The Dissertation of Jacob Martin Pasner
is approved:

Professor Jason Nielsen, Chair

Professor Abraham Seiden

Professor Michael Hance

Dean Lori Kletzer
Vice Provost and Dean of Graduate Studies

Copyright © by

Jacob Martin Pasner

2019

31 **Table of Contents**

32	List of Figures	vii
33	List of Tables	x
34	Abstract	xi
35	Dedication	xii
36	Acknowledgments	xiii
37	1 Introduction	1
38	I Theoretical Motivations and the Standard Model	2
39	2 The Standard Model and Beyond	3
40	2.1 The Standard Model	4
41	2.1.1 Bosons	5
42	2.1.2 Fermions	8
43	2.2 Quantum Electrodynamics	8
44	2.3 Quantum Chromodynamics	12
45	2.4 The Higgs Mechanism	14

46	2.4.1	Electroweak Symmetry Breaking	14
47	2.4.2	Fermion Mass Terms	18
48	2.4.3	The Higgs Boson	19
49	3	Boosted Higgs at the LHC	21
50	3.1	Physics beyond the Standard Model	22
51	3.2	Higgs Production Mechanisms	22
52	3.3	Branching Ratios	22
53	3.4	Discovery	22
54	3.5	Fermion Decay Modes	22
55	3.6	Boosted Higgs	22
56	II	Experimental Apparatus and Associated Facilities	23
57	4	The Large Hadron Collider	24
58	4.1	Particle Injection Chain	25
59	4.2	LHC layout and design	27
60	4.3	Performance	30
61	4.4	Pile-up at the LHC	32
62	5	The ATLAS Detector	34
63	5.1	ATLAS Coordinate System	37
64	5.2	Tracking with the Inner Detector	41
65	5.2.1	Pixel Detector	43
66	5.2.2	Semiconductor Tracker	43
67	5.2.3	Transition Radiation Tracker	44
68	5.3	Calorimetry	45

69	5.3.1 Electromagnetic Calorimeter	46
70	5.3.2 Hadronic Calorimeter	48
71	5.4 Muon Spectrometer	50
72	III The HbbISR Analysis	53
73	6 Data and Simulation Preparation	54
74	6.1 Data Used	54
75	6.2 Monte Carlo Samples	54
76	7 Physics Object Selection	55
77	7.1 Calorimeter Jets	56
78	7.2 Track Jets	56
79	7.3 Fat Jets	56
80	7.4 B-tagged Jets	56
81	7.5 Muons	56
82	7.6 Overlap Removal	56
83	8 Event Selection	57
84	8.1 Selected Triggers	57
85	8.2 Pre-selection Studies	57
86	8.3 Signal Selection	57
87	8.4 Optimisation	57
88	9 Background Estimation	58
89	9.1 Multi-jet QCD estimation	58
90	9.2 $t\bar{t}$ control region	58
91	9.3 Single top estimation	58

92	9.4 Hadronic vector boson channel	58
93	10 Systematic Uncertainties	59
94	10.1 Theoretical Uncertainties	59
95	10.2 Experimental Uncertainties	59
96	11 Statistical Fit	60
97	11.1 Profile Likelihood Function	60
98	11.2 Fit Configuration	60
99	11.3 Statistical Tests	60
100	12 Results	61
101	12.1 Expectations	61
102	12.2 Statistical Analysis Results	61
103	12.3 Measurements and Limits	61
104	IV Conclusion	62
105	13 Conclusion	63
106	Bibliography	63
107	A Hadronic Vqq Sherpa Studies	66

108 List of Figures

109	2.1	Summary of several Standard Model total and fiducial production cross	
110		section measurements, corrected for leptonic branching fractions, com-	
111		pared to the corresponding theoretical expectations. All theoretical ex-	
112		pectations were calculated at NLO or higher. The dark-color error bar	
113		represents the statistical uncertainty. The lighter-color error bar repre-	
114		sents the full uncertainty, including systematics and luminosity uncer-	
115		tainties. The data/theory ratio, luminosity used and reference for each	
116		measurement are also shown. Uncertainties for the theoretical predictions	
117		are quoted from the original ATLAS papers. They were not always eval-	
118		uated using the same prescriptions for PDFs and scales. The Wgamma	
119		and Zgamma theoretical cross-sections have non-perturbative corrections	
120		applied to the NNLO fixed order calculations (PRD 87, 112003 (2013)).	
121		Not all measurements are statistically significant yet.	6
122	2.2	Table of all observed fundamental particles of the current Standard Model.	7
123	2.3	A lower dimensionality representation of the shape of the Higgs Potential.	
124		The central peak represents a $v = 0$ rotationally symmetric unstable	
125		state, while the trough represents the infinite choices of minima that can	
126		be selected upon the spontaneous breaking of symmetry.	15
127	4.1	CERN accelerator complex	26
128	4.2	Labeled diagram of all the experiments at the LHC indicating the counter	
129		circulating beams and points of interest along the circumference of the	
130		accelerator.	28
131	4.3	Depiction of a LHC dipole magnet 2-in-1 design labeling the major com-	
132		ponents	29

133	4.4	Luminosity is monitored as both a running total known as the Integrated	
134		Luminosity as depicted in (a) and as an instantaneous quantity as shown	
135		in (b)	32
136	4.5	Pileup for data taking periods 2015 - 2018	33
137	5.1	[3] Here we see a cut-away side view of the ATLAS detector with the	
138		major components labeled. Note that within each of these labeled com-	
139		ponents there may exist multiple different detector technologies. For scale	
140		two people in red are shown standing between the disk muon chambers	
141		on the left side of the figure.	35
142	5.2	This slice of the ATLAS detector depicts how different particles interact	
143		with each component of the detector it crosses. A dashed line indicates	
144		no interaction while a solid line indicates interaction. Electrons (yel-	
145		low/green) and charged hadrons (red) interact with the tracker and curve	
146		in the solenoid's magnetic field. Electrons and photons (yellow/green) are	
147		absorbed by the Electromagnetic calorimeter. All hadrons (red/yellow)	
148		are absorbed by the Hadronic calorimeter. The muons (orange) curve in	
149		both the solenoid and torroid magnetic fields before exiting the detector.	
150		Finally, the neutrinos (white) pass through the entire detector without	
151		interacting.	38
152	5.3	[4] A cartoon view of the the LHC from above showing the SPS, LHC	
153		and the four main experiments of the LHC: ATLAS, CMS, LHCb, and	
154		ALICE. The standard cartesian coordinate system is shown with its origin	
155		at the ATLAS interaction point, the positive x -axis towards the center	
156		of the LHC, the positive y -axis pointing upwards, and the positive z -axis	
157		pointing along the beamline towards the "A-side"	39
158	5.4	Modified from [4] this cartoon represents a selection of pseudorapidity	
159		(η) values overlaid with some cartesian coordinates (dashed black lines).	
160		The redlines are drawn for $\eta = \pm 0.5, 1.0, 3.0$	40
161	5.5	[5] Diagram of inner detector	41
162	5.6	[8] Schematic of the Inner Detector including eta lines. Each component	
163		shown is cylindrically symmetric leading to a multi-layered detector. . .	42
164	5.7	[3] A cutaway diagram of ATLAS's sampling calorimeters	45
165	5.8	[3] Sketch of LAr EMC barrel module where the lead and liquid argon	
166		layers are visible in an accordion like geometry. Looking from the fore-	
167		ground to the back there are 3 different types of cells visible.	47

168	5.9	[3] Schematic of a tile calorimeter module including a depiction of the con-	
169		nection between the scintillator tile to the photomultiplier via a wavelength-	
170		shifting fibre.	49
171	5.10	[3] A cut-away diagram of the ATLAS muon system and its many sub-	
172		detectors.	51

173 List of Tables

Abstract

An Inclusive Search for the decay of a Boosted Higgs boson in the $H \rightarrow b\bar{b}$

channel with the ATLAS detector

by

Jacob Martin Pasner

Abstract placeholder

180

Dedication

181

Dedication

182

Dedication

Acknowledgments

184 Chapter 1

185 Introduction

186 Every dissertation should have an introduction. You might not realize it, but the
187 introduction should introduce the concepts, backgrouand, and goals of the dissertation.

188

Part I

189

Theoretical Motivations and the

190

Standard Model

Chapter 2

The Standard Model and Beyond

The Standard Model (SM) of Particle Physics is humanities best "guess" at the force laws that describe the observed behavior of all particles in our universe. Its formulation is a collection of Quantum Field Theories (QFT) that describe the following interactions of elementary matter in Nature: the electromagnetic force, the weak nuclear force and the strong nuclear force. Gravity is noticeably absent as currently there is no viable quantum theory for observed gravitational effects. The Glashow-Salam-Weinberg (GSW) theory of Quantum Electrodynamics (QED) describes the electromagnetic and weak forces, while Quantum Chromodynamics (QCD) describes the strong force. These theories form the following symmetry group of the Standard Model.

$$\underbrace{\mathrm{SU}_C(3)}_{\mathrm{QCD}} \otimes \underbrace{\mathrm{SU}_L(2) \otimes \mathrm{U}_Y(1)}_{\mathrm{GSW}}. \quad (2.1)$$

202 The gauge principle states that the SM Lagrangian and its predictions must be invariant
203 under local transformations using an operator from any of these constituent groups.
204 Thus, any theory must only include transformations and terms that maintain the local
205 invariance of the complete Lagrangian. In particular, this requirement was violated
206 by any attempt to include an explicit mass term for the Gauge Bosons of QED and
207 for all fermions. Around 1960 a possible solution to this lack of mass was proposed
208 in the form of the spontaneous breaking of the ElectroWeak symmetry, now known as
209 the Higgs mechanism. In the following sections I will go into more detail about the
210 Lagrangian formalism of the Standard Model, QCD, QED and this recently verified
211 Higgs Mechanism.

212 **2.1 The Standard Model**

213 At the turn of the 20th century our understanding of the constituent matter of the uni-
214 verse was limited to what we could see with microscopes and imply from the observations
215 of light and electricity, giving us evidence for both the photon and the electron. In the
216 first half of the century we discovered the field of subatomic physics with Rutherford's
217 1911 gold foil scattering experiment, and Dirac successfully demonstrated the quantiza-
218 tion of the electromagnetic field, the first step towards a fully Gauge Invariant Quantum
219 Field Theory. In the second half we literally delved deeper, discovering that the nucleus
220 contained structure and extended our theories to include the the complex mechanics of
221 quarks and gluons. With the discovery of the Higgs in 2013 the Standard Model has

222 become an irrefutable framework as can be seen in the high level of agreement between
223 theory and experiment in figure 2.1.

224 The QCD and QED theories predict two classes of particles: fermions and bosons shown
225 in figure 2.2. These particles represent the quanta of the quantum fields of the Standard
226 Model and the mediators of the fundamental forces of Nature.

227 2.1.1 Bosons

228 These spin-1 particles are known as the vector gauge bosons and are the force carriers
229 of the SM. The most commonly known is the electromagnetic force's un-charged and
230 massless photon (γ) which interacts with all charged particles and is often referred to
231 as "light". The weak nuclear force is involved in nuclear interactions such as beta
232 decays and is carried by 3 bosons all of which have mass and couple to all fermions;
233 the W^\pm bosons, which mediate the charged weak nuclear interaction and allow for
234 flavor changing currents; and the Z boson which mediates the neutral weak nuclear
235 interaction. Finally we have 8 massless gluons which mediate the strong nuclear force
236 and only interact with fermions with a "color" charge such as the quarks contained
237 inside the nucleus. The only spin-0 boson, the Higgs Boson (h) is the key to generating
238 mass terms in the SM Lagrangian for the massive Gauge Bosons and for fermions. This
239 is done through the so called Higgs Mechanism and is discussed in more detail in section
240 2.4.

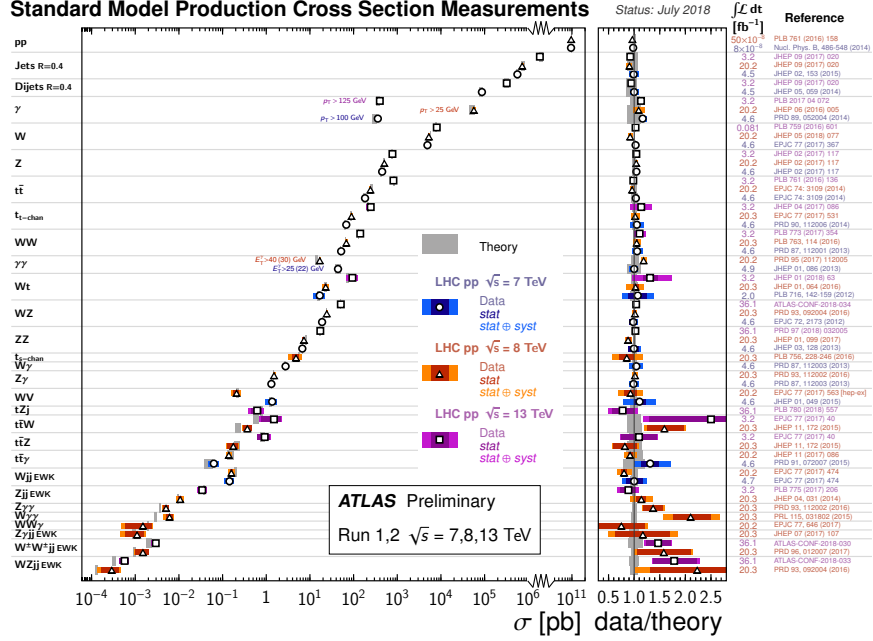


Figure 2.1: Summary of several Standard Model total and fiducial production cross section measurements, corrected for leptonic branching fractions, compared to the corresponding theoretical expectations. All theoretical expectations were calculated at NLO or higher. The dark-color error bar represents the statistical uncertainty. The lighter-color error bar represents the full uncertainty, including systematics and luminosity uncertainties. The data/theory ratio, luminosity used and reference for each measurement are also shown. Uncertainties for the theoretical predictions are quoted from the original ATLAS papers. They were not always evaluated using the same prescriptions for PDFs and scales. The $W\gamma$ and $Z\gamma$ theoretical cross-sections have non-perturbative corrections applied to the NNLO fixed order calculations (PRD 87, 112003 (2013)). Not all measurements are statistically significant yet.

Standard Model of Elementary Particles


















three generations of matter (fermions)						interactions / force carriers (bosons)	
QUARKS	I	II	III				
	<div><div>mass charge spin</div><div>$\approx 2.2 \text{ MeV}/c^2$ $\frac{2}{3}$ $\frac{1}{2}$</div><div> u up</div></div>	<div><div>$\approx 1.28 \text{ GeV}/c^2$ $\frac{2}{3}$ $\frac{1}{2}$</div><div> c charm</div></div>	<div><div>$\approx 173.1 \text{ GeV}/c^2$ $\frac{2}{3}$ $\frac{1}{2}$</div><div> t top</div></div>	<div><div>0 0 1</div><div> g gluon</div></div>	<div><div>$\approx 124.97 \text{ GeV}/c^2$ 0 0 0</div><div> H higgs</div></div>		
	<div><div>$\approx 4.7 \text{ MeV}/c^2$ $-\frac{1}{3}$ $\frac{1}{2}$</div><div> d down</div></div>	<div><div>$\approx 96 \text{ MeV}/c^2$ $-\frac{1}{3}$ $\frac{1}{2}$</div><div> s strange</div></div>	<div><div>$\approx 4.18 \text{ GeV}/c^2$ $-\frac{1}{3}$ $\frac{1}{2}$</div><div> b bottom</div></div>	<div><div>0 0 1</div><div> γ photon</div></div>			
	LEPTONS	<div><div>$\approx 0.511 \text{ MeV}/c^2$ -1 $\frac{1}{2}$</div><div> e electron</div></div>	<div><div>$\approx 105.66 \text{ MeV}/c^2$ -1 $\frac{1}{2}$</div><div> μ muon</div></div>	<div><div>$\approx 1.7768 \text{ GeV}/c^2$ -1 $\frac{1}{2}$</div><div> τ tau</div></div>	<div><div>$\approx 91.19 \text{ GeV}/c^2$ 0 0 1</div><div> Z Z boson</div></div>		
<div><div>$< 2.2 \text{ eV}/c^2$ 0 $\frac{1}{2}$</div><div> ν_e electron neutrino</div></div>		<div><div>$< 0.17 \text{ MeV}/c^2$ 0 $\frac{1}{2}$</div><div> ν_μ muon neutrino</div></div>	<div><div>$< 18.2 \text{ MeV}/c^2$ 0 $\frac{1}{2}$</div><div> ν_τ tau neutrino</div></div>	<div><div>$\approx 80.39 \text{ GeV}/c^2$ ± 1 1</div><div> W W boson</div></div>			
				SCALAR BOSONS			
				GAUGE BOSONS VECTOR BOSONS			

Figure 2.2: Table of all observed fundamental particles of the current Standard Model.

241 **2.1.2 Fermions**

242 These spin-1/2 particles can be further broken up into two distinct families of particles,
243 the leptons and the quarks, both of which contain three "generations" each with an "up"
244 and "down" type particle. The leptons "up" type members are the electrically charged
245 electron (e), muon (μ) and tau (τ) while the "down" type are their electrically neutral
246 counterparts ν_e , ν_μ , ν_τ . The quarks "up" type members are the up (u), charm (c),
247 and top (t) each with a $+2/3$ elementary charge, while the "down" type members are
248 the down (d), strange (s), and bottom (b) all of which have a $-1/3$ elementary charge.
249 Each quark carries a "color" charge thus allowing them to participate in strong force
250 interactions. Due to the observed color confinement of the strong force these quarks are
251 only observed in colorless bound states known as "mesons" (1 quark and 1 anti-quark)
252 and "baryons" (an odd number of quarks and anti-quarks). All of the above fermions
253 have an anti-particle partner which has the opposite electrical charge but is otherwise
254 identical.

255 **2.2 Quantum Electrodynamics**

256 In the SM the Electromagnetic and Weak nuclear forces are unified into the Electroweak
257 interaction which is represented by the $SU(2)_L \times U(1)_Y$ gauge group. The L represents
258 the physical observable that the Weak interaction, and thus the $SU(2)$ transformation,
259 only acts on left handed particle states. The Y states that this is the $U(1)$ symmetry

for the weak hypercharge Y instead of the electromagnetic charge. The particle states for these interactions are solutions to the Dirac equation and are represented as Dirac spinor doublets (Ψ_L) for the left handed states, and as Dirac spinor singlets (Ψ_R) for the right handed states. Thus when a general transformation from the Electroweak gauge group is applied to the left handed spinor doublet you get equation 2.2

$$\Psi_L \rightarrow \Psi'_L = \exp \left(\underbrace{ig' \frac{Y_L}{2} \zeta(x)}_{U(1)_Y} + \underbrace{ig_W \boldsymbol{\alpha}(x) \cdot \mathbf{T}}_{SU(2)_L} \right) \Psi_L. \quad (2.2)$$

For the right handed spinor singlet the $SU(2)_L$ doesn't contribute and you get equation 2.3

$$\Psi_R \rightarrow \Psi'_R = \exp \left(\underbrace{ig' \frac{Y_R}{2} \zeta(x)}_{U(1)_Y} \right) \Psi_R. \quad (2.3)$$

We can see that these local gauge transformations have introduced space-time dependent terms $\boldsymbol{\alpha}(x)$ and $\zeta(x)$ into our electroweak Lagrangian. Due to the derivatives contained within the kinetic term of this lagrangian, this new configuration would introduce additional terms, thus violating our required local gauge invariance. Luckily, we can remove these additional terms by replacing the standard derivative (∂_μ) with the covariant derivative (D_μ) as seen in equation 2.4 for the left handed states and 2.5 for the right handed states.

$$D_\mu = \partial_\mu - \underbrace{\frac{1}{2}ig' B_\mu Y_L}_{U(1)_Y} - \underbrace{\frac{1}{2}ig_W \mathbf{W}_\mu \cdot \boldsymbol{\tau}}_{SU(2)_L} \quad (2.4)$$

$$D_\mu = \partial_\mu - \underbrace{\frac{1}{2}ig' B_\mu Y_R}_{U(1)_Y} \quad (2.5)$$

274 Here we see two new gauge fields; B_μ the weak hypercharge field and \mathbf{W}_μ the charged
 275 weak field as well as the associated coupling constants g', g_W, Y_L, Y_R and the $SU(2)$
 276 generators $\boldsymbol{\tau}$. Next we right down the transformation properies of these new fields

$$\mathbf{W}_\mu(x) \rightarrow \mathbf{W}'_\mu(x) = \mathbf{W}_\mu + \partial_\mu \boldsymbol{\alpha}(x) + g \mathbf{W}_\mu(x) \times \boldsymbol{\alpha}(x) \quad (2.6)$$

$$B_\mu \rightarrow B'_\mu = B_\mu + \frac{1}{g'} \partial_\mu \zeta(x) \quad (2.7)$$

277 The form of these fields is choosen such that the final Lagrangian is invariant under
 278 $SU(2)_L \times U(1)_Y$ transformations, and thus we have restored gauge invariance for the
 279 kinetic term of our electroweak Lagrangian! Inserting these new definitions into the
 280 Lagrangian for the spinor field Ψ which satisfies the free-particle Dirac equation we get

$$\mathcal{L} = i\bar{\Psi}_L \gamma^\mu \left(\partial_\mu - \frac{1}{2}ig' B_\mu Y_L - \frac{1}{2}ig_W \mathbf{W}_\mu \cdot \boldsymbol{\tau} \right) \Psi_L + i\bar{\Phi}_R \gamma^\mu \left(\partial_\mu - \frac{1}{2}ig' B_\mu Y_R \right) \Phi_R \quad (2.8)$$

281 Next we must construct the gauge field self interaction and mass terms

$$\mathcal{L} = -\frac{1}{4}\mathbf{F}_{\mu\nu}\mathbf{F}^{\mu\nu} - \frac{1}{4}B_{\mu\nu}B^{\mu\nu} + \frac{1}{2}M_W^2\mathbf{W}_\mu\mathbf{W}^\mu + \frac{1}{2}M_B^2B_\mu B^\mu \quad (2.9)$$

282 where the field tensors $\mathbf{F}^{\mu\nu}$ and $B^{\mu\nu}$ are defined to be

$$\mathbf{F}^{\mu\nu} = \partial^\mu\mathbf{W}^\nu - \partial^\nu\mathbf{W}^\mu + g\mathbf{W}^\mu \times \mathbf{W}^\nu \quad (2.10)$$

$$B^{\mu\nu} = \partial^\mu B^\nu - \partial^\nu B^\mu \quad (2.11)$$

283 The field tensor terms in equation 2.9 are invariant under our gauge transformations,
 284 but simply plugging in equation 2.4 or equation 2.5 into the mass terms shows that
 285 these terms violate gauge invariance thus implying $M_W = 0$ and $M_B = 0$ in direct
 286 contradiction of the observed masses of the weak gauge bosons. This issue arises again
 287 for fermion mass terms as illustrated below for the electron field (e) expanded in its chiral
 288 basis.

$$m_e\bar{e}e = m_e \begin{pmatrix} e_R^\dagger & e_L^\dagger \end{pmatrix} \begin{pmatrix} e_L \\ e_R \end{pmatrix} = m_e(e_R^\dagger e_L + e_L^\dagger e_R) \quad (2.12)$$

289 Remembering that the left and right handed spinors of the electroweak interaction trans-
 290 form differently we see that this mixture of right and left fields violates gauge invariance.
 291 This again forces us to conclude that $m_e = 0$ in contradiction to the observation that

the electron does indeed have mass. As mentioned in section 2.1.1 the resolution to these mass mysteries lies in the Higgs mechanism discussed in section 2.4

2.3 Quantum Chromodynamics

Quantum Chromodynamics is the continuation of the mathematical framework established by Quantum Electrodynamics (section 2.2, this time for the strong force described by the $SU(3)_C$ gauge group where the C represents the "color" charge of QCD. This color charge doesn't imply actual visible color, but is useful as an analogy to the visible spectrum where a combination of red, green, and blue generates white. For QCD the combination of red, green, and blue color charges results in a colorless object. As mentioned in section 2.1.2 the quarks will contain a color (anti-color) charge represented by a color triplet field which transforms under the general $SU(3)$ transformation as shown here

$$q = \begin{pmatrix} q_r \\ q_g \\ q_b \end{pmatrix} \rightarrow q' = \exp \left(ig_s \sum_{k=1}^8 \eta_k(x) \frac{\lambda_k}{2} \right) q \quad (2.13)$$

Here the λ_k are the generators for $SU(3)$, $\eta(x)_k$ is the space-time dependancy for each generator, and g_s is the strong coupling constant. As with QED, the introduction of these space-time dependant terms introduces new terms into the kinematic portion of

307 the lagrangian thus spoiling our gauge invariance. Again, we introduce a covariant
 308 derivative to restore invariance

$$D_\mu = \partial_\mu - ig_s G_\mu^k \frac{\lambda_k}{2} \quad (2.14)$$

309 Here the G_μ^k are the new fields introduced for the 8 gluons. These new fields transform
 310 under $SU(3)$ as shown in equation 2.15

$$G_\mu^k \rightarrow G_\mu'^k = G_\mu^k + \partial_\mu \eta_k(x) + g_s f_{klm} \eta_l(x) G_\mu^m \quad (2.15)$$

311 Given these definitions we can construct the QCD Lagrangian (\mathcal{L}_{QCD}) as shown in
 312 equation 2.16 where the gluon field tensor $G_k^{\mu\nu}$ is the one defined in equation 2.17

$$\mathcal{L}_{QCD} = \bar{q}(i\gamma_\mu D^\mu - m_q)q - \frac{1}{4} G_k^{\mu\nu} G_{k\mu\nu} \quad (2.16)$$

$$G_k^{\mu\nu} = \partial^\mu G_k^\nu - \partial^\nu G_k^\mu + g_s f_{klm} G_l^\mu G_m^\nu \quad (2.17)$$

313 The strong force is peculiar in that we experimentally observe only colorless objects in
 314 the form of bound states of quarks known as hadrons. Qualitatively, when a bound
 315 state of quarks (meson or baryon) is given sufficient energy to separate the strong force
 316 dramatically increases in strength. At the point where the objects would separate, and

317 thus no longer be colorless, it becomes energetically favorable to produce a quark/anti-
 318 quark pair in a process known as hadronization. In other words, attempting to separate
 319 a bound quark state into its colored constituents simply results in new colorless bound
 320 states. This requirement of colorless objects by the strong force is known as color
 321 confinement. For highly energetic strong interactions at hadron colliders the result is
 322 an expanding chain of hadronizing quarks and gluons and their decay products known
 323 as a jet.

324 **2.4 The Higgs Mechanism**

325 The Higgs Mechanism is the system by which the gauge bosons and fermions attain mass
 326 through the spontaneous breaking of the electroweak symmetry of the Higgs potential.
 327 This section will also discuss briefly the couplings of the Higgs boson to massive particles,
 328 as well as it's self couplings.

329 **2.4.1 Electroweak Symmetry Breaking**

330 The Higgs field is expressed as a complex doublet, Φ , and thus has four components as
 331 shown in equation 2.18

$$\Phi(x) = \begin{pmatrix} \phi^+ \\ \phi^0 \end{pmatrix} = \frac{1}{\sqrt{2}} \begin{pmatrix} \phi_1(x) + i\phi_2(x) \\ \phi_3(x) + i\phi_4(x) \end{pmatrix} \quad (2.18)$$

332 The four components of this field each represent a degree of freedom which will be
 333 used to give the longitudinal polarizations of the gauge bosons W^\pm, Z and the mass of
 334 the Higgs boson. The resulting lagrangian for the higgs includes a kinetic term (K) as
 335 well as the Higgs potential (V) all of which are invariant under the Electroweak gauge
 336 symmetry $SU(2)_L \times U(1)_Y$

$$\mathcal{L}_{\text{Higgs}} = \underbrace{(D_\mu \Phi)^\dagger D^\mu \Phi}_{\text{K}} - \underbrace{(\mu^2 \Phi^\dagger \Phi + \lambda (\Phi^\dagger \Phi)^2)}_{\text{V}} \quad (2.19)$$

337 Here we constrain $\mu^2 < 0$ and $\lambda > 0$ such that the potential forms a stable minima. The
 338 shape of this potential is shown in figure 2.3 and is often referred to as the "Mexican-hat"
 339 or "Wine-bottle" potential.

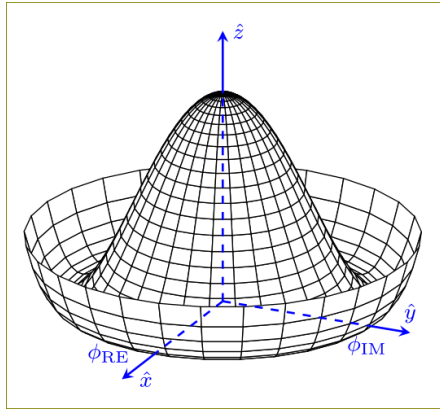


Figure 2.3: A lower dimensionality representation of the shape of the Higgs Potential. The central peak represents a $v = 0$ rotationally symmetric unstable state, while the trough represents the infinite choices of minima that can be selected upon the spontaneous breaking of symmetry.

340 Whatever you call it, this potential is significant in that its minimum is not at $\Phi = 0$
 341 but instead is symmetric around the origin thus defining an infinite number of states
 342 that minimize V . The value of this minima can be calculated by taking the derivative
 343 of V with respect to Φ and setting it equal to 0. This value, also known as the vacuum
 344 expectation value (vev) has been found to be $v \equiv \sqrt{-\mu^2/\lambda} = 246$ GeV. In order to reach
 345 this ground state energy, the Higgs field must spontaneously break this symmetry, and
 346 thus acquire an arbitrary single value. For ease of calculation we orient our coordinate
 347 system such that

$$\langle \Phi(x) \rangle = \frac{1}{\sqrt{2}} \begin{pmatrix} 0 \\ v \end{pmatrix} \quad (2.20)$$

348 Next we parameterize small perturbations around the minimum of the Higgs potential
 349 as

$$\langle \Phi(x) \rangle = \frac{1}{\sqrt{2}} \begin{pmatrix} 0 \\ v + h(x) \end{pmatrix} \exp \left(i \frac{\tau^i}{2} \theta^i(x) \right) \quad (2.21)$$

350 Here the real scalar field $h(x)$ corresponds to radial perturbations of the minima and
 351 while the three $\theta^i(x)$ are the Nambu-Goldstone fields with values determined by your
 352 choice of gauge. Choosing the unitary gauge of $\theta^i(x) = 0$ and expanding the kinetic

353 term of equation 2.19 around the vev we get

$$\mathcal{L}_{\text{Higgs},K} = \frac{g^2 v^2}{8} \left((W_\mu^-)^\dagger W^{-\mu} + (W_\mu^+)^\dagger W^{+\mu} \right) + \frac{1}{2} \begin{pmatrix} W_\mu^{3\dagger} & B_\mu^\dagger \end{pmatrix} \mathbf{M}^2 \begin{pmatrix} W^{3\mu} \\ B^\mu \end{pmatrix} + \dots \quad (2.22)$$

354 Here the first term is the physical mass term for the W^\pm bosons where we have con-
 355 structed their charge eigenstates out of the $W^{1,2}$ fields like this $W^\pm = \frac{1}{\sqrt{2}}(W^1 \mp iW^2)$.
 356 The second term represents the mixture of the W^3 and B fields through the mass ma-
 357 trix \mathbf{M} . By diagonalizing this matrix and identifying the mass eigenstates we find the
 358 physical fields of the photon (γ) and the Z boson

$$\mathbf{M}_{\text{Diagonalized}}^2 = \begin{pmatrix} 0 & 0 \\ 0 & \frac{v^2}{4}(g^2 + g'^2) \end{pmatrix} \quad (2.23)$$

359 The upper left diagonal element corresponds to the massless photon while the lower
 360 right diagonal element gives the mass of the massive Z boson. This leaves us with the
 361 following masses for the 4 Electroweak bosons

$$m_W = \frac{1}{2}gv \quad , \quad m_Z = \frac{1}{2}v\sqrt{g^2 + g'^2} \quad , \quad m_\gamma = 0 \quad (2.24)$$

362 The masses of the W^\pm and Z gauge bosons can be related through the Weinberg angle

363 or mixing angle which

$$\theta_W = \cos^{-1} \left(\frac{g}{\sqrt{g^2 + g'^2}} \right) \rightarrow m_Z = \frac{m_W}{\cos \theta_W} \quad (2.25)$$

364 Using this definition we can write out the exact mixture of B and W^3 that make up the
365 photon and Z boson

$$\gamma = \cos(\theta_W)B + \sin(\theta_W)W^3 \quad (2.26)$$

$$Z = -\sin(\theta_W)B + \cos(\theta_W)W^3 \quad (2.27)$$

366 2.4.2 Fermion Mass Terms

367 In section 2.2 we saw that fermion mass terms violate gauge invariance due to the
368 mixing of the left and right chiral states. The Higgs mechanism again allows for a gauge
369 invariant method of generating mass terms but this time through the Yukawa coupling
370 of the Higgs field to the fermion fields. To see an example of this here is the Yukawa
371 coupling term for the electron doublet (Ψ_L) and singlet (Ψ_R) coupling to the Higgs
372 field (Φ) after spontaneous symmetry breaking giving it the form shown in equation
373 2.21 where we have again chosen the unitary gauge $\Phi^i(x) = 0$.

$$\mathcal{L}_{Yukawa} = -g_e \left[\bar{\Psi}_L \Phi \Psi_R + \bar{\Psi}_R \Phi^\dagger \Psi_L \right] \quad (2.28)$$

$$= -\frac{g_e}{\sqrt{2}} \left[\begin{pmatrix} \bar{\nu}_e & \bar{e} \end{pmatrix}_L \begin{pmatrix} 0 \\ \nu + h \end{pmatrix} e_R + \bar{e}_R \begin{pmatrix} 0 & (\nu + h) \end{pmatrix} \begin{pmatrix} \nu_e \\ e \end{pmatrix}_L \right] \quad (2.29)$$

$$= -\underbrace{\frac{g_e}{\sqrt{2}} \nu}_{m_e} (\bar{e}_L e_R + \bar{e}_R e_L) - \underbrace{\frac{g_e}{\sqrt{2}} h}_{g_{e,h}} (\bar{e}_L e_R + \bar{e}_R e_L) \quad (2.30)$$

374 And voila, we have successfully generated mass terms for our fermion field and main-
 375 tained the gauge invariance of our Lagrangian by using all gauge invariant fields. This
 376 operation has also left us with the second term which represents the coupling of the
 377 electron to the higgs itself thus giving us the form of it's coupling constant $g_{e,h}$. Using
 378 our newly found mass of the electron m_e we can write

$$g_{e,h} = \frac{g_e}{\sqrt{2}} = \frac{m_e}{\nu} \quad (2.31)$$

379 Thus we see that the coupling of the higgs boson to a fermion is indeed proportional to
 380 the mass of the fermion itself. In other words, the more massive a particle is, the more
 381 the higgs couples to it and vice versa.

382 2.4.3 The Higgs Boson

383 As we have seen this Higgs mechanism not only properly mixes the gauge fields thus
 384 providing them gauge invariant mass terms, it also properly combines the left and right

385 chiral states of fermions to produce their mass terms. The final step then is to determine
 386 an observable of the theory that can be tested in experiment, namely the existence of a
 387 massive scalar particle, the Higgs boson itself.

388 Turning our attention to the potential term (V) of equation 2.19 and substituting in
 389 our definition for Φ given in equation 2.21 we find

$$\mathcal{L}_{\text{Higgs,V}} = \frac{1}{2}\mu^2\nu^2 - \mu^2h^2 + \lambda\nu h^3 + \frac{1}{4}\lambda h^4 \quad (2.32)$$

390 Here the first term is constant and thus can be ignored. The second term is the mass
 391 term for the SM particle the Higgs boson, $m_h = \sqrt{-2\mu^2} = \sqrt{2\lambda}\nu$. Remembering that
 392 $h = h(x)$ was used for small radial perturbations of the Higgs field from its minimum
 393 we can identify the Higgs boson simply as an excitation of the Higgs field. Finally, the
 394 third and fourth terms represent the Higgs boson self-couplings. With these couplings
 395 and mass terms in hand we can now move on to the experimental verification of this
 396 theory as discussed next in chapter 3.

397 Chapter 3

398 Boosted Higgs at the LHC

399 Its July 4th, 2012 and the walls of building 500 are reverberating as Particle Physicists
400 around the world rejoice the discovery of the particle that gives all things mass, the
401 Higgs Boson.

402 **3.1 Physics beyond the Standard Model**

403 **3.2 Higgs Production Mechanisms**

404 **3.3 Branching Ratios**

405 **3.4 Discovery**

406 **3.5 Fermion Decay Modes**

407 **3.6 Boosted Higgs**

408

Part II

409

Experimental Apparatus and

410

Associated Facilities

411 Chapter 4

412 The Large Hadron Collider

413 Located 100 meters under the Swiss / French boarder lies the 26.7 kilometer Large
414 Hadron Collider (LHC) [1]. The culmination of a huge international collaboration,
415 this apparatus is used to produce proton and heavy ion collisions for observation by the
416 four major experiments at the LHC: ATLAS, CMS, LHCb, and ALICE. The system was
417 designed for a maximum center-of-mass energy of $\sqrt{s} = 14$ TeV and a peak instantaneous
418 luminosity of $L = 10^{34} \text{cm}^{-2} \text{s}^{-1}$.

419 The first LHC workshop was held in 1984 in Lausanne at the European Organization
420 for Nuclear Reserach (CERN) [2]. The nearly 30 year old case for a machine that
421 would push towards the discovery of the elusive Higgs Boson was presented using the
422 existing CERN accerlerator facilities and the Large Electron Positron (LEP) collider
423 tunnel. The proposal became reality on September 10, 2008 when the first proton beams
424 were circulated, only to have calamity strike 9 days later in the form of a catastrophic

425 electrical fault. The repairs and improvements lasted until November 2009 when the
426 LHC restarted. Since then this modern marvel has worked wonderfully and, as hoped,
427 lead to the discovery of the Higgs Boson by the CMS and ATLAS collaborations July
428 4, 2013.

429 The following chapter provides a brief introduction to the worlds most powerful accel-
430 erator starting with the little red bottle of hydrogen in building XXX, and ending with
431 the interaction point where protons collide at the highest energies ever produced.

432 4.1 Particle Incjecton Chain

433 We begin with the most common element in the Universe, hydrogen, as our source of
434 protons. A bottle of hydrogen gas provides 100 microsecond pulses of raw H_2 which
435 is then injected into a Duoplasmatron. There, a strong electric field and free elctrons
436 from a cathode ionize the molecule into bare H^+ aka a proton! These protons are
437 then accelerated by a 90kV field, leaving the Duoplasmatron with 1.4% speed of light
438 ($\sim 4000\text{km/s}$) or, in relativistic units, about 83KeV. The bare protons are then fed
439 into the accelerating RadioFrequency (RF) cavities of Linear Accelerator 2 (LINAC2).
440 Inside, conductors charged by a powerful oscillating electromagnetic field accelerate the
441 protons resulting in a 50MeV energy. Along the way, small quadrupole magnets shape
442 the proton packet insuring they remain in a tight beam. This pattern of accleration
443 with RF cavities and shaping/turnig with magnets is then repeated with CERN's first

The diagram illustrates the LHC and its associated accelerators and experiments. The LHC is the largest circular accelerator, with two main rings. The SPS (Super Proton Synchrotron) is a smaller circular accelerator located below the LHC. The PS (Proton Synchrotron) is a circular accelerator located below the SPS. The LINAC2 and LINAC3 are linear accelerators located at the bottom left. The LEIR (Large Electron Ion Ring) is a circular accelerator located at the bottom right. The AD (Antiproton Decelerator) is a linear accelerator located in the West Area. The COMPASS experiment is located in the North Area. The ALICE experiment is located in the West Area. The ATLAS experiment is located in the West Area. The CMS experiment is located in the North Area. The LHC-b experiment is located in the East Area. The CNGS (Compact Neutrino Generator) is located in the East Area. The Gran Sasso (I) is located at the bottom right, 730 km from the LHC. The diagram also shows the West Area, North Area, and East Area. The LHC is labeled with 'LHC' in the center. The SPS is labeled with 'SPS' in the center. The PS is labeled with 'PS' in the center. The LINAC2 and LINAC3 are labeled with 'LINAC2' and 'LINAC3' respectively. The LEIR is labeled with 'LEIR' in a green box. The AD is labeled with 'AD' in a blue box. The COMPASS experiment is labeled with 'COMPASS'. The ALICE experiment is labeled with 'ALICE'. The ATLAS experiment is labeled with 'ATLAS'. The CMS experiment is labeled with 'CMS'. The LHC-b experiment is labeled with 'LHC-b'. The CNGS is labeled with 'CNGS'. The Gran Sasso (I) is labeled with 'Gran Sasso (I) 730 km'. The diagram also shows the West Area, North Area, and East Area. The LHC is labeled with 'LHC' in the center. The SPS is labeled with 'SPS' in the center. The PS is labeled with 'PS' in the center. The LINAC2 and LINAC3 are labeled with 'LINAC2' and 'LINAC3' respectively. The LEIR is labeled with 'LEIR' in a green box. The AD is labeled with 'AD' in a blue box. The COMPASS experiment is labeled with 'COMPASS'. The ALICE experiment is labeled with 'ALICE'. The ATLAS experiment is labeled with 'ATLAS'. The CMS experiment is labeled with 'CMS'. The LHC-b experiment is labeled with 'LHC-b'. The CNGS is labeled with 'CNGS'. The Gran Sasso (I) is labeled with 'Gran Sasso (I) 730 km'. The diagram also shows the West Area, North Area, and East Area.

Rudolf LEY, PS Division, CERN, 02.09.96
Revised and adapted by Antonella Del Rosso, ETT Div.,
in collaboration with B. Desforges, SL Div., and
D. Manglunki, PS Div. CERN, 23.05.01

26

444 synchrotron, the Proton Synchrotron (PS) rendering a 1.4 GeV beam. The final step
445 before the LHC comes with the Super Proton Synchrotron where the same technologies
446 are implemented to produce 450 GeV protons, ready for injection into the LHC. A
447 diagrammatic representation of this chain can be seen in figure 4.1

448 In order to produce proton-proton collisions the LHC uses two beams circulating in
449 opposite directions. The beams are not continuous, but instead consist of bunches, or
450 buckets, of $\mathcal{O}(10^{11})$ protons with a spacing of 25ns. Given the LHC circumference this
451 allows for 3564 buckets, however only 2808 are filled per beam due to safety requirements
452 and injection limitations. Each beam takes 4 minutes and 20 seconds to fill and then an
453 additional 20 minutes to for the protons to reach their maximum energy of 7 TeV TeV,
454 or 99.99999991% the speed of light! Under normal operating conditions these beams
455 can be used for many hours.

456 4.2 LHC layout and design

457 While often depicted as a perfect circle the LHC is in reality an octagon with rounded
458 edges, called arcs, as can be seen in figure 4.2. Here you can see the counter circulating
459 beams of protons depicted in red and blue. These beams are focused and collided at
460 the 4 dedicated interaction points at rates of up to 40 MHz. Two of these points are
461 occupied by the ATLAS and CMS experiments, both of which are high luminosity,
462 multi-purposed experiments.

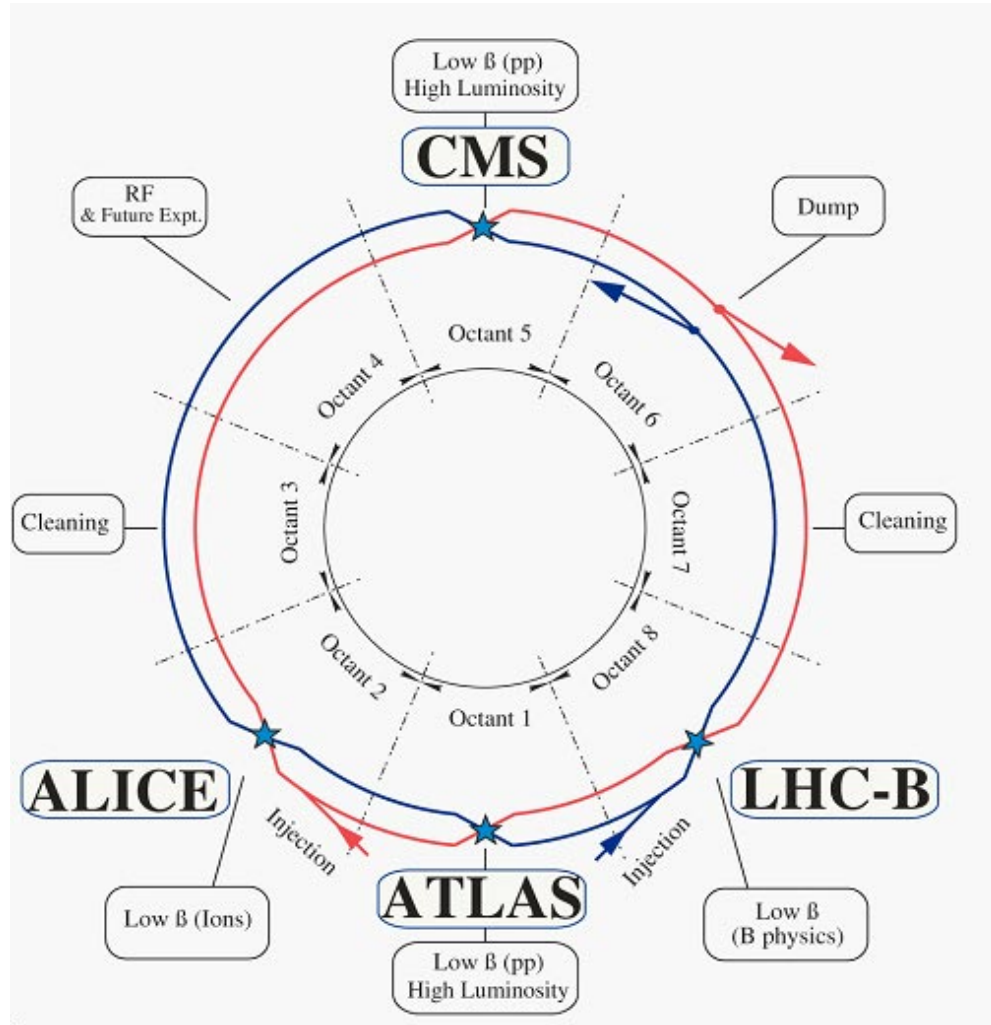


Figure 4.2: Labeled diagram of all the experiments at the LHC indicating the counter circulating beams and points of interest along the circumference of the accelerator.

463 The exact design of the tunnel is due to the experimental constraints of the original
 464 machine for which it was built, the Large Electron Positron (LEP) Collider. For the
 465 $\sim 2,000$ times lighter electron the maximum energy was limited by the synchrotron
 466 radiation, proportional to $\frac{1}{m^4}$, requiring long straight sections of accelerating RF cavities
 467 to recouperate the lost energy. Given that this effect is $\mathcal{O}(10^{13})$ times smaller for the
 468 proton the LHC is instead limited by our ability to design and construct magnets strong
 469 enough to bend the beam given the already determined curvature of the 8 arcs.

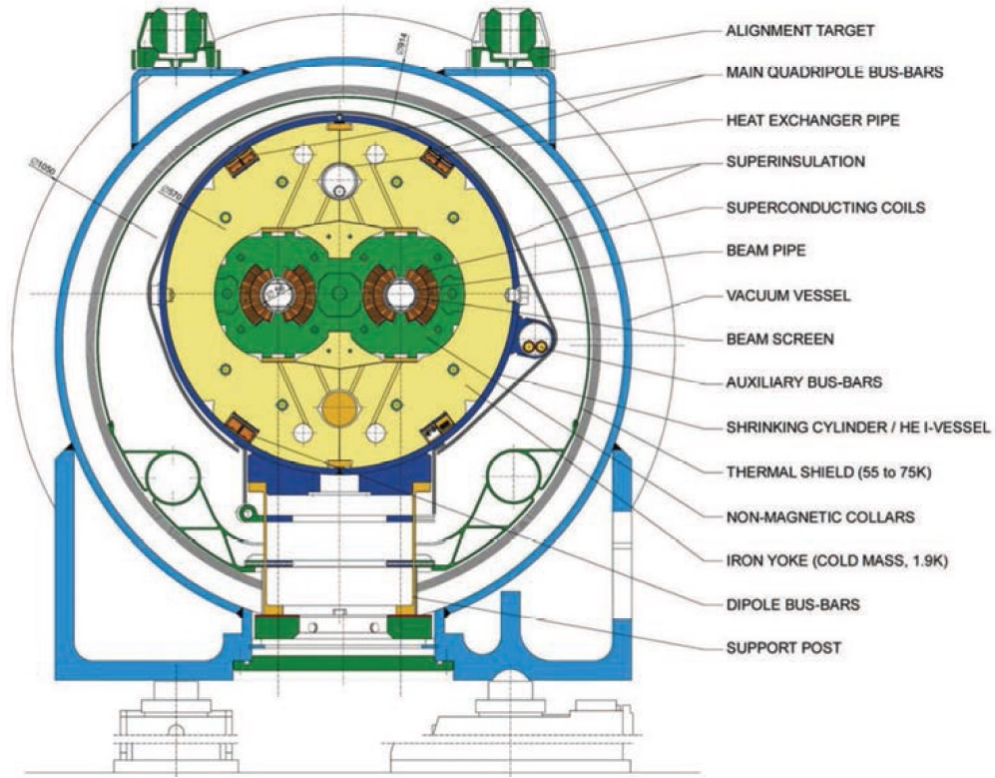


Figure 4.3: Depiction of a LHC dipole magnet 2-in-1 design labeling the major components

470 The oppositely circulating beams must each have their own ring and magnetic field
471 which lead to the creation of a twin-bore (i.e. "two-in-one") magnet design, a cross
472 section of which can be seen in figure 4.3. These magnets are constructed using NbTi
473 superconductors which are cooled to 2K using superfluid helium. These magnets are
474 designed to provide the needed 8.33 T magnetic field required to bend the beams at the
475 design beam energy of 7 TeV. In total 1231 of these 15 m long bending dipole magnets
476 are used, in association with 392 5-7m long quadrupole magnets which are responsible
477 for keeping the proton bunches in a tight beam by squeezing them either horizontally
478 or vertically.

479 **4.3 Performance**

480 Since the begining of its stable running in 2010 the LHC has performed well, even
481 exceeding our expectations. While the experiment itself is incredibly complex, the
482 performance of the machine, for the purposes of our analysis, can be reduced to two
483 numbers; the familiar center of mass energy of the beams and a less common quantity
484 known as the integrated luminosity.

485 For particle physics the integrated luminosity is proportional to the total number of
486 collisions recorded during a specified time period, while the instantaneous luminosity is
487 proportional to the bunch crossing rate along with the cross section of a proton-proton
488 interaction and represents the potential number of collisions per second. Knowing this

we can see that the integrated luminosity, L_{int} is simply the integral of the instantaneous luminosity $L_{inst.}$ for a choosen data period as seen in equation 4.1.

$$L_{int} = \int L_{inst.} dt \quad (4.1)$$

For a standard Gaussian beam, $L_{inst.}$ can be written as

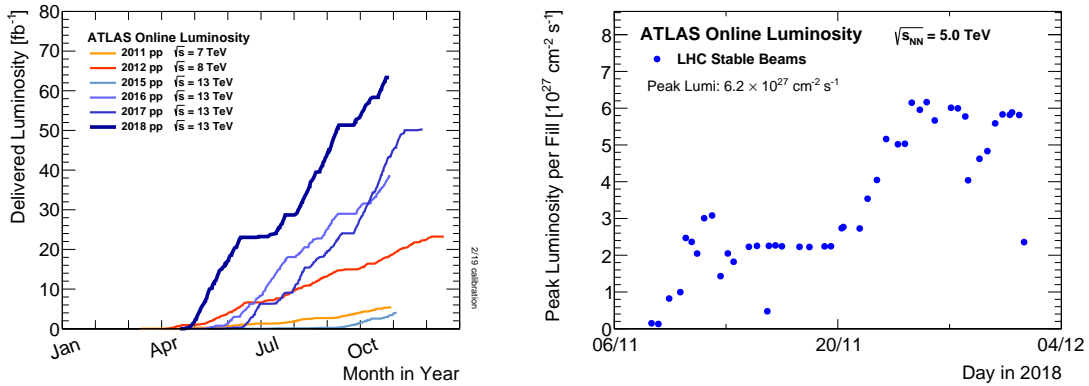
$$L = \frac{N_b^2 n_b f_{rev} \gamma_r}{4\pi \epsilon_n \beta^*} F \quad (4.2)$$

where N_b is the number of particles per bunch, n_b the number of bunches per beam, f_{rev} the revolution frequency, γ_r the relativistic gamma factor, ϵ_n the normalized transverse beam emittance, β^* the beta function at the collision point, and F the geometric luminosity reduction factor due to the crossing angle at the interaction point given by

$$F = \left(1 + \left(\frac{\theta_c \sigma_z}{2\sigma^*} \right)^2 \right)^{-1/2} \quad (4.3)$$

where θ_c is the full crossing angle at the interaction point, σ_z is the RMS bunch length, and σ^* is the transverse RMS beam size at the interaction point.

For the ATLAS experiment the integrated luminosity for each year can be seen in figure 4.4a as well as an example of the instantaneous luminosity for the choosen year in figure 4.4b.



(a) Integrated Luminosity 2011 - 2018 (b) 2018 Peak Instantaneous Luminosity

Figure 4.4: Luminosity is monitored as both a running total known as the Integrated Luminosity as depicted in (a) and as an instantaneous quantity as shown in (b)

4.4 Pile-up at the LHC

Given the large number of protons per bunch and the cross-section of a proton-proton interaction, the probability to observe multiple interactions per bunch crossing is quite high. These multiple-interaction are known as pile-up, μ or the time averaged representation $\langle\mu\rangle$, and come in two different forms:

1. **In-time pile-up:** These are the other proton-proton collisions that occur during the same bunch crossing as the primary interaction that caused the Data Acquisition (DAQ) system to trigger. These are the standard extra interactions we expect to observe as stated above.
2. **Out-of-time pile-up:** These are interactions that occur either before or after a

511 bunch crossing that causes the DAQ to trigger. This effect is generally due to the
 512 long integration times of some detector electronics.

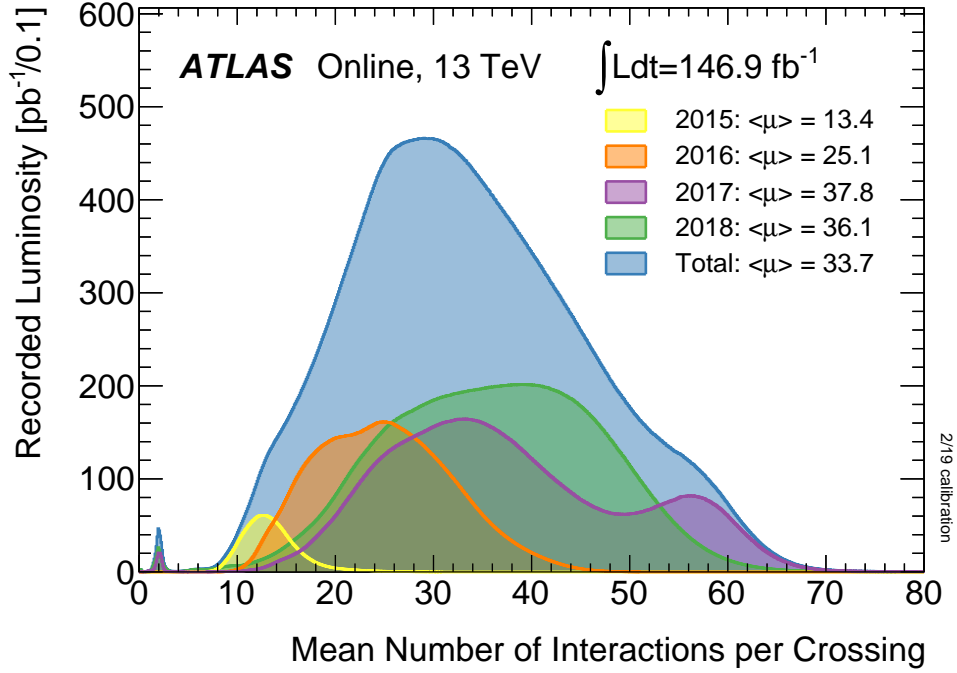


Figure 4.5: Pileup for data taking periods 2015 - 2018

513 The pile-up profile for past years can be seen in figure 4.5. The width of this distributino
 514 is due a combination of Poissonian statistics, the decrease in number of protons per bunch
 515 over the lifetime of a single run, and optimization tweaks to the beam's profile during
 516 runtime. Understanding and eliminating the noise from these pile-up events is crucial
 517 to reconstructing physics variables to represent the primary interaction we hope to
 518 observe.

519 Chapter 5

520 The ATLAS Detector

521 Given the immense energies available at the LHC, and the veritable zoo of particles we
522 are trying to detect, we require a general-purpose experiment in order to fully exploit
523 the full range of physics opportunities provided. Two international collaborations rose
524 to this challenge, the CMS (Compact Muon Solenoid) and ATLAS (A Toroidal LHC
525 Apparatus) experiments. While both have similar physics goals and each of them
526 strengths and weaknesses, this dissertation will focus on the ATLAS experiment and
527 the intricacies of its three main sub-detectors and two massive magnet systems depicted
528 in figure 5.1.

529 Originally proposed in 1994 the ATLAS experiment was completed in 2008. On July
530 4th, 2012 in a joint announcement the ATLAS and CMS experiments announced the
531 discovery of the long predicted Higgs Boson. The collaboration now boasts over 3000
532 physicists from 175 institutions spread across 38 countries and continues to probe

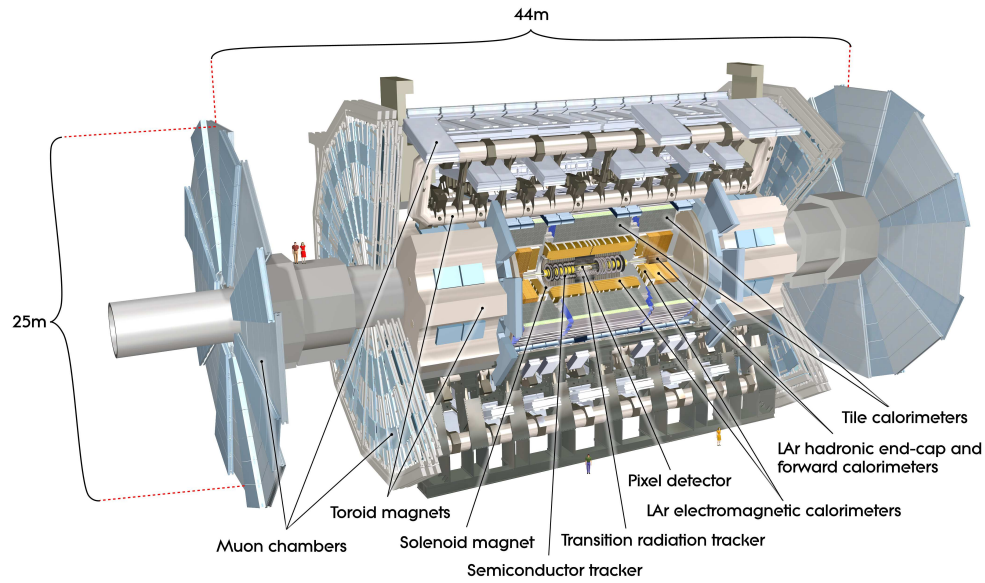


Figure 5.1: [3] Here we see a cut-away side view of the ATLAS detector with the major components labeled. Note that within each of these labeled components there may exist multiple different detector technologies. For scale two people in red are shown standing between the disk muon chambers on the left side of the figure.

533 the limits of the Standard Model in pursuit of answers to some of Humanities deepest
534 questions.

535 Located approximately 100 meters underground in a vast excavated chamber, the AT-
536 LAS detector rests its 7000 metric tonnes on a bed of concrete reinforced steel. Out of
537 it flows the signals of over 100 million electronic channels through a zip tied mass of
538 greater than 3000 kilometers of cabling. At its very center is one of the four interaction
539 points of the LHC, specifically Point 1, where the two counter circulating proton beams
540 are skillfully shaped and then collided by a series of magnets. The energetic particles
541 resultant from this collision then fly out in all directions into the bulk of the ATLAS
542 detector.

543 The first sub-system they meet is the Inner Detector (ID) and its many layers of strip
544 and pixel silicon detectors along with a transition radiation gaseous wire detector, all
545 bathed in the 2T magnetic field of the surrounding superconducting solenoidal magnet.
546 This system exploits the ionization of charged particles to track their curved trajectory
547 through the magnetic field. This curvature gives us charge information, a momentum
548 measurement, and precision 3D vertices crucial to the identification of the secondary
549 vertices of a b-hadron decay.

550 Outside of the solenoid the particles are faced with first the Electromagnetic and then
551 the Hadronic sampling calorimeters. Here, layers of scintillator and high radiation length
552 materials are implemented to measure the energy of electrons, photons, and hadrons.
553 As the goal is to completely absorb the energy of all outgoing particles the calorimeter

554 has a nearly 4π solid angle coverage.

555 Finally we have the muon system surrounding the calorimeter and equipped with its
556 own torroidal magnet system. Here the charged muon bends in the magnetic field
557 while leaving a trail of ionization in the muon spectrometer before exiting the detector
558 completely. Neutrinos are the only other standard model particle that leave the detector,
559 however they do so without detection. A depiction of the various particle interactions
560 with the different detector sub-systems can be seen in figure 5.2

561 In the following sections I will explain our choosen coordinate system and give a more
562 detailed reveiw of these 3 detector sub-systems.

563 **5.1 ATLAS Coordinate System**

564 Using the nominal interaction point as the origin, ATLAS uses a right handed coor-
565 dinate system where the positive x -axis points towards the center of the LHC ring,
566 the positive y -axis points upwards, and the positive z -axis is defined by the counter
567 clockwise circulating beam direction as viewed from above shown in figure 5.3 [3].

568 Using these coordinates we can define the physical momentum of the objects measured
569 as $\vec{p} = (p_T, p_z)$ with p_T being the momentum of the object in the transverse plane and
570 p_z the momentum along the beam axis. Given the cylindrical symmetry of ATLAS it
571 is desireable to define the polar angle θ from the beam axis with the $r - \phi$ plane being
572 perpendicular to that axis. Since the particles we observe are relativistically boosted

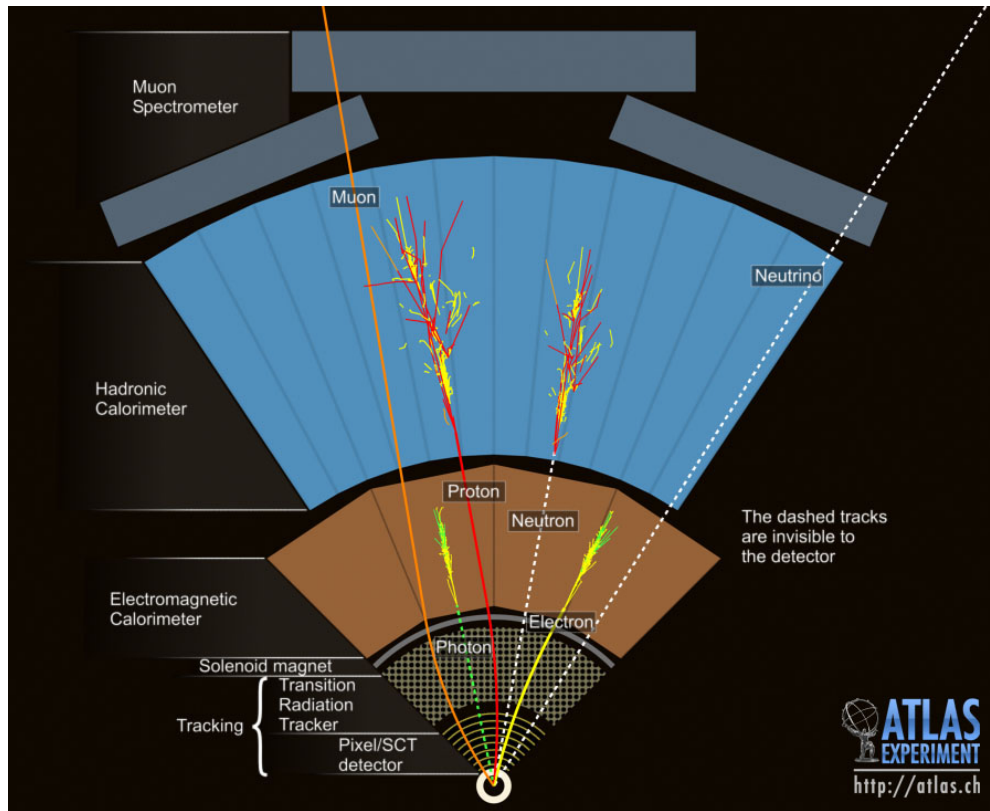


Figure 5.2: This slice of the ATLAS detector depicts how different particles interact with each component of the detector it crosses. A dashed line indicates no interaction while a solid line indicates interaction. Electrons (yellow/green) and charged hadrons (red) interact with the tracker and curve in the solenoid's magnetic field. Electrons and photons (yellow/green) are absorbed by the Electromagnetic calorimeter. All hadrons (red/yellow) are absorbed by the Hadronic calorimeter. The muons (orange) curve in both the solenoid and torroid magnetic fields before exiting the detector. Finally, the neutrinos (white) pass through the entire detector without interacting.

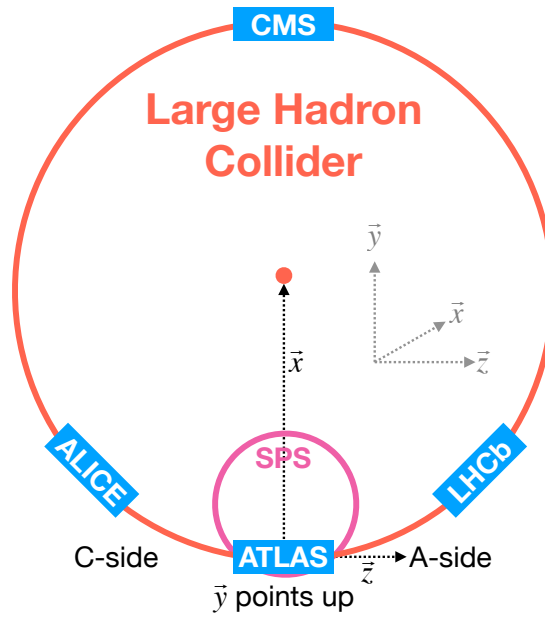


Figure 5.3: [4] A cartoon view of the the LHC from above showing the SPS, LHC and the four main experiments of the LHC: ATLAS, CMS, LHCb, and ALICE. The standard cartesian coordinate system is shown with its origin at the ATLAS interaction point, the positive x -axis towards the center of the LHC, the positive y -axis pointing upwards, and the positive z -axis pointing along the beamline towards the "A-side"

573 in the z -axis it is desirable to use the Lorentz invariant quantity pseudorapidity (η)
 574 defined in terms of the polar angle by

$$\eta = -\ln \tan \left(\frac{\theta}{2} \right). \quad (5.1)$$

575 where $\eta = 0$ is in the $x - y$ plane and larger values of $|\eta|$ being closer to the beam axis
 576 as can be seen in figure 5.4.

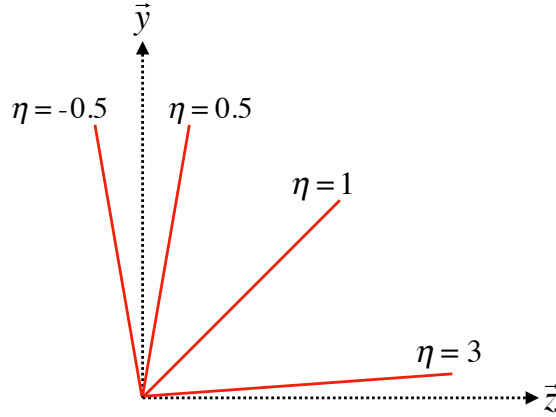


Figure 5.4: Modified from [4] this cartoon represents a selection of pseudorapidity (η) values overlaid with some cartesian coordinates (dashed black lines). The redlines are drawn for $\eta = \pm 0.5, 1.0, 3.0$

577 In this analysis the angular separation between objects in the detector is calculated and
 578 represented using the geometric quantity

$$\Delta R = \sqrt{(\Delta\eta)^2 + (\Delta\phi)^2} \quad (5.2)$$

5.2 Tracking with the Inner Detector

With its closest component, the insertable b-layer (IBL) [5], only 3.3 cm from the interaction point The Inner Detector (ID), shown in figure 5.5 [6, 7], faces the incredible challenge of providing precision momentum resolution and identification of both primary and secondary vertex measurements of charged tracks all while receiving the highest fluence.

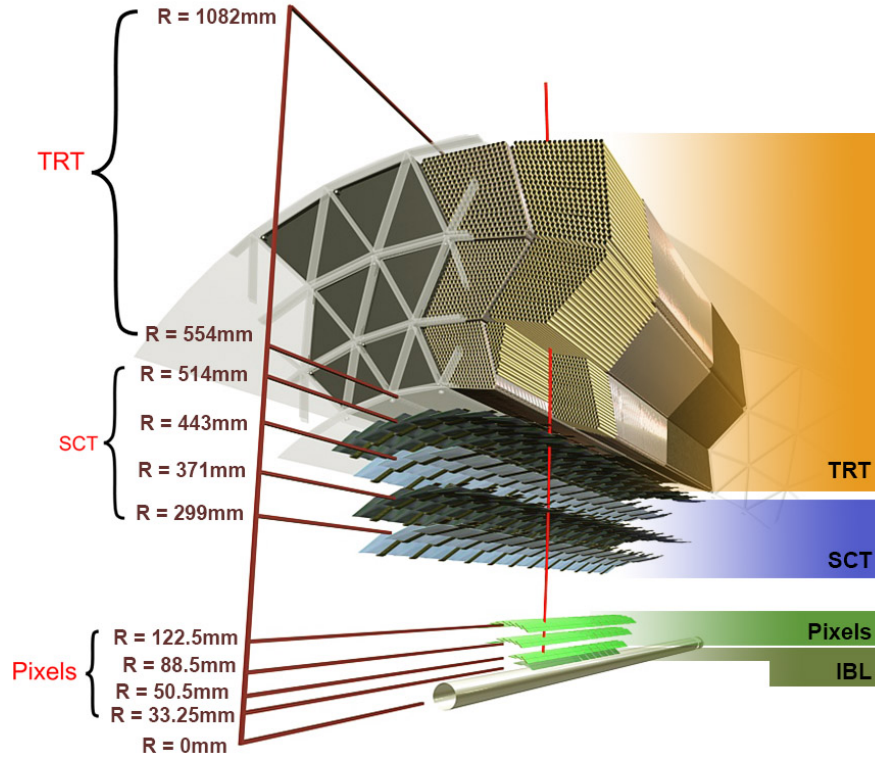


Figure 5.5: [5] Diagram of inner detector

It is designed to be very compact to reduce the probability of a particle decaying inside and to give precision measurements of the particles curvature in the 2T solenoidal

587 magnetic field. This leads to excellent momentum resolution above the nominal p_T
 588 threshold of 0.5 GeV and within the pseudorapidity range of $|\eta| < 2.5$ as shown in figure
 589 5.6

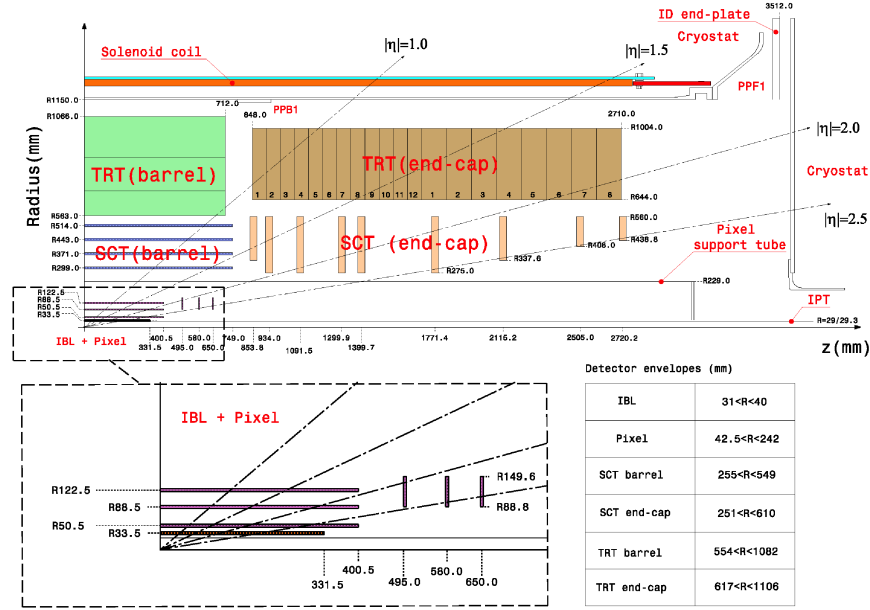


Figure 5.6: [8] Schematic of the Inner Detector including eta lines. Each component shown is cylindrically symmetric leading to a multi-layered detector.

590 The ID is composed of three different detector technologies for particle trajectory re-
 591 construction: The Pixel Detector, Semiconductor Tracker (SCT) and the Transition
 592 Radiation Tracker (TRT). These will be discussed in the following sections.

593 5.2.1 Pixel Detector

594 The ATLAS Pixel Detector [3], the innermost subdetector of the ID, is designed to
595 give the best resolution possible as close as possible to the interaction point. This
596 is accomplished using the 4 barrel layers and the 3 disks per endcap as indicated in
597 figure 5.6. The inner most barrel layer, the IBL, has pixel dimensions of $50\mu\text{m}(\hat{\phi}) \times$
598 $250\mu\text{m}(\hat{z}) \times 200\mu\text{m}(\hat{r})$. For the other layers the dimensions are $50\mu\text{m}(\hat{\phi}) \times 400\mu\text{m}(\hat{z})$ for
599 about 90% of the pixels and $50\mu\text{m}(\hat{\phi}) \times 600\mu\text{m}(\hat{z})$ for the others, all with a thickness
600 of $250\mu\text{m}(\hat{r})$. This gives a total active area of 1.88m^2 collected through 92.4 million
601 readout channels, more than half of the total number of channels for ATLAS. This
602 detailed charged particle information very close to the interaction point is crucial not
603 only for pattern recognition for track reconstruction, but also for the reconstruction
604 of the primary and secondary vertices intrinsic to the decay of a b -hadrons, a critical
605 element of the analysis presented in this thesis.

606 5.2.2 Semiconductor Tracker

607 Encompassing the Pixel Detector, the Semiconductor Tracker (SCT) [3] is composed of
608 double sided silicon microstrips modules. Each side of the 4088 modules is constructed
609 out of two silicon strip sensors that are daisy chained together. The result is 768
610 composite strips each 12.6cm with an inter-strip pitch of $80\mu\text{m}$. In the barrel the strips
611 are aligned with the \hat{z} direction, while in the end caps they are aligned with the \hat{r}
612 direction. In both cases the separation of the strips is constant in $\hat{\phi}$. The two sides are

613 rotated with respect to each other by $40\mu\text{m}$ to allow for position measurement along the
 614 length of the strip. These modules are then used to tile the 4 barrel layers and 9 disks
 615 per endcap (18 disks in total) as seen in figure 5.6. This design is chosen to ensure
 616 that each charged track interacts with 8 strip layers (equivalent to four space points).
 617 This information is used to further measure the momentum and impact parameter, and
 618 as well as vertex identification of charged particles.

619 **5.2.3 Transition Radiation Tracker**

620 The Transition Radiation Tracker [3], the outermost subdetector of the ID, provides
 621 tracking through the detection of transition radiation from ultra-relativistic charged
 622 particles for $\eta < 2.0$ using 350,000 drift tube channels also known as straws. The
 623 4mm diameter straws are filled with a 70% Xe, 27% CO₂, and 3% O₂ gas mixture
 624 and a $31\mu\text{m}$ diameter gold-plated tungsten wire anode at the center for the collection
 625 of the ionization signal. In the barrel 73 azimuthally symmetric layers of 144cm straws
 626 are oriented parallel to the beam pipe with an electrical division in the center of each
 627 allowing the two sides to be read out separately. For each endcap the straws are radially
 628 oriented in 160 symmetric planes each containing 768 37cm long drift tubes shown
 629 in figure 5.6. In both the barrel and the end caps polypropylene fibers (barrel) or
 630 foils (encaps) function as the transition radiation material which causes the relativistic
 631 charged particles to radiate and thus ionize the gas in the straw. The amount of
 632 transition radiation produced is proportional to the Lorentz factor meaning that lighter

633 particles (e.g. electrons) will produce more radiation. Thus, by defining a high and low
 634 threshold, we can identify tracks belonging to electrons by requiring they register more
 635 high-threshold hits. There are typically 36 TRT hits per charged track.

636 5.3 Calorimetry

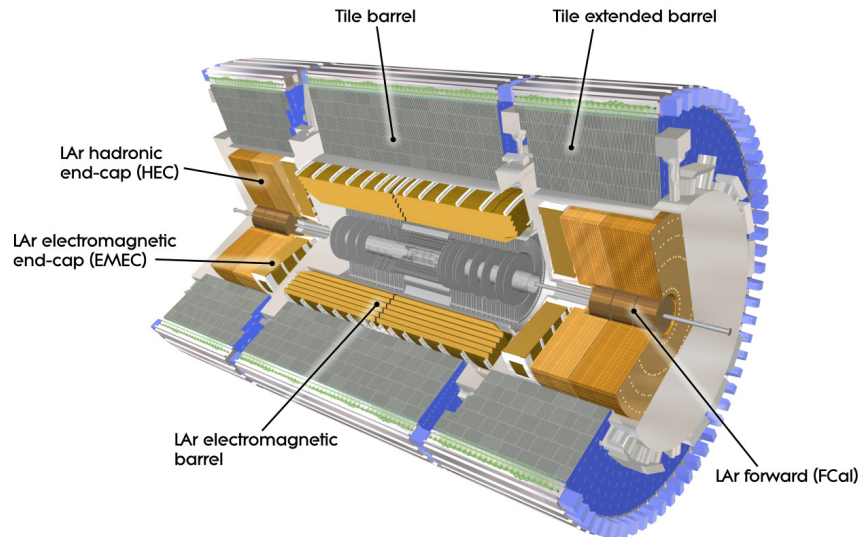


Figure 5.7: [3] A cutaway diagram of ATLAS's sampling calorimeters

637 Once the proton collision remnants have passed through the ID and it's surround-
 638 ing solenoid they enter into the ATLAS calorimeters depicted in figure 5.7. Sampling
 639 calorimeter technologies were choosen for their compact geometry and lower cost point.
 640 These are constructed by alternating layers of absorber, a dense material which reduces
 641 the incedent particles energy, and active material which produces a detectible signal
 642 when a partilce passes through. This means that the detected signal is only a fraction

643 of the total energy of the particle and thus requires a study of the calorimeter response
 644 for calibration purposes [9]. The first system, the Electromagnetic Calorimeter (EMC),
 645 is designed to measure the energy of electrons and photons which primarily lose their
 646 energy via bremsstrahlung and pair production electromagnetic interactions. Outside of
 647 the EMC is the Hadronic Calorimeter (HC) which is designed to measure the energy of
 648 jets of hadrons through their electromagnetic and strong interactions. These detectors
 649 cover the entire $|\eta| < 4.9$ range and provide complete containment of both Electromag-
 650 netic and Hadronic showers with higher granularity in the EMC for $|\eta| < 2.5$, the region
 651 matched to the ID, for precision measurements of electrons and photons. By instrument-
 652 ing this huge space in $|\eta|$ we can search for events with asymmetric energy deposits which
 653 imply the existence of a particle we didn't detect represented by missing transverse
 654 energy E_T^{miss} .

655 **5.3.1 Electromagnetic Calorimeter**

656 The innermost calorimeter, the Liquid Argon (LAr) Electromagnetic Calorimeter (EMC)
 657 [3], uses lead as the absorber and liquid argon as the active material in an "accordion
 658 geometry" as seen in figure 5.8. This geometry was chosen for uniform coverage in
 659 $\hat{\phi}$ due to its lack of un-instrumented cracks in the radial direction. The barrel region
 660 covers $|\eta| < 1.475$ and an end cap on each side covers $1.375 < |\eta| < 3.2$ each housed
 661 in their own cryostat. The barrel is composed of two half barrels with a 4mm gap at
 662 $z = 0$ and both end caps are divided into an inter wheel covering $2.5 < |\eta| < 3.2$ and

an outer wheel covering $1.375 < |\eta| < 2.5$.

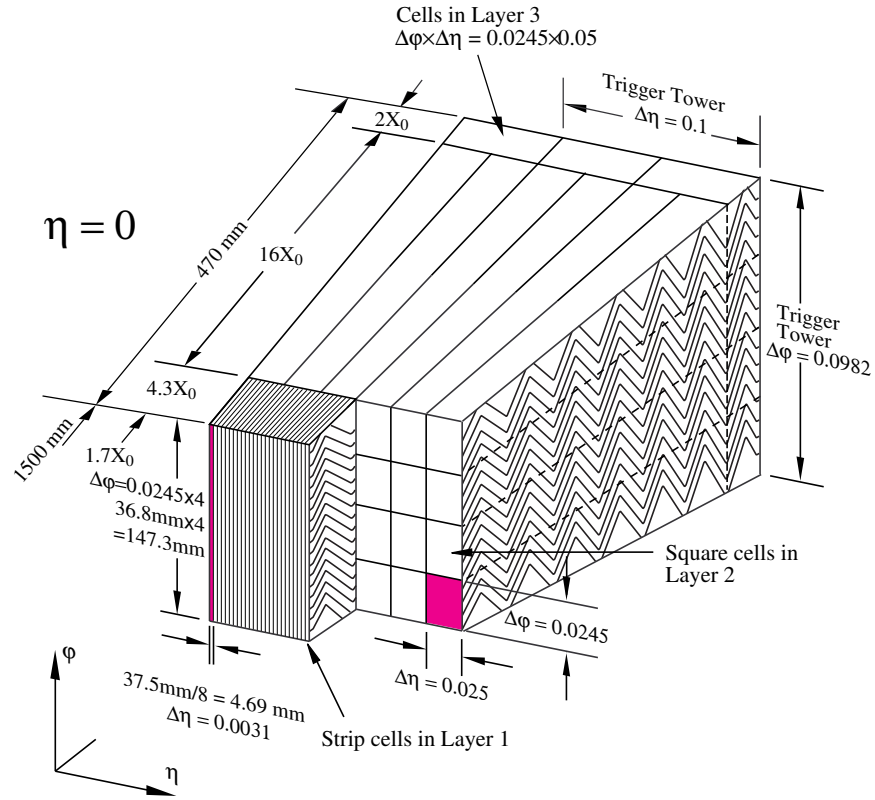


Figure 5.8: [3] Sketch of LAr EMC barrel module where the lead and liquid argon layers are visible in an accordion like geometry. Looking from the foreground to the back there are 3 different types of cells visible.

In the $|\eta| < 2.5$ region the EMC has 3 radial layers for precision physics measurements. Layer 1 consists of strip cells which are finely segmented with $\Delta\eta = 0.0031$ and $\Delta\phi = 0.0245$ allowing for precision position resolution which gives discrimination power between a single γ deposit and the π^0 characteristic $\gamma\gamma$ deposit. Layer 2, which collects the largest fraction of energy from electromagnetic shower, is segmented with

669 $\Delta\eta = .025$ and $\Delta\phi = 0.0245$. Layer 3 collects the tail of the electromagnetic shower
 670 using a coarser segmentation of $\Delta\eta = .05$ and $\Delta\phi = 0.0245$. Additionally, in the region
 671 $|\eta| < 1.8$ a thin pre-sampler, which contains no lead absorber, was placed in front of
 672 Layer 1 to allow for energy corrections due to losses upstream of the EMC. Combined
 673 the EMC is > 22 radiation lengths (X_0) in the barrel and $> 24 X_0$ in the end-caps,
 674 where a radiation length is the average distance an electron travels in a given material
 675 before losing $1/e$ of its original energy E_0 via bremsstrahlung radiation.

676 5.3.2 Hadronic Calorimeter

677 Directly outside the EMC envelope is the Hadronic Calorimeter (HC) system [3] which
 678 consists of three sampling calorimeter technologies: the Tile calorimeter, the LAr
 679 hadronic end-cap calorimeter (HEC) and the LAr forward calorimeter (FCal). Com-
 680 bined, these three subsystems give measurements of hadronic jet energies in the $0 <$
 681 $|\eta| < 4.9$ range. The tile calorimeter uses steel as the absorber layer and scintillating
 682 tiles as the active material and covers the region $|\eta| < 1.7$ with a barrel section flanked
 683 by two barrel extensions each divided azimuthally into 64 modules. These scintillator
 684 tiles are read out on two sides by wave-length shifting fibers connected to photomul-
 685 tiplier tubes as seen in figure 5.9. At $\eta = 0$ the total tile calorimeter thickness is 9.7
 686 nuclear interaction lengths (λ), where λ is the average distance a hadron travels before
 687 interacting inelastically with a nucleus.

688 The HEC is composed of two independent wheels per end-cap located just past the

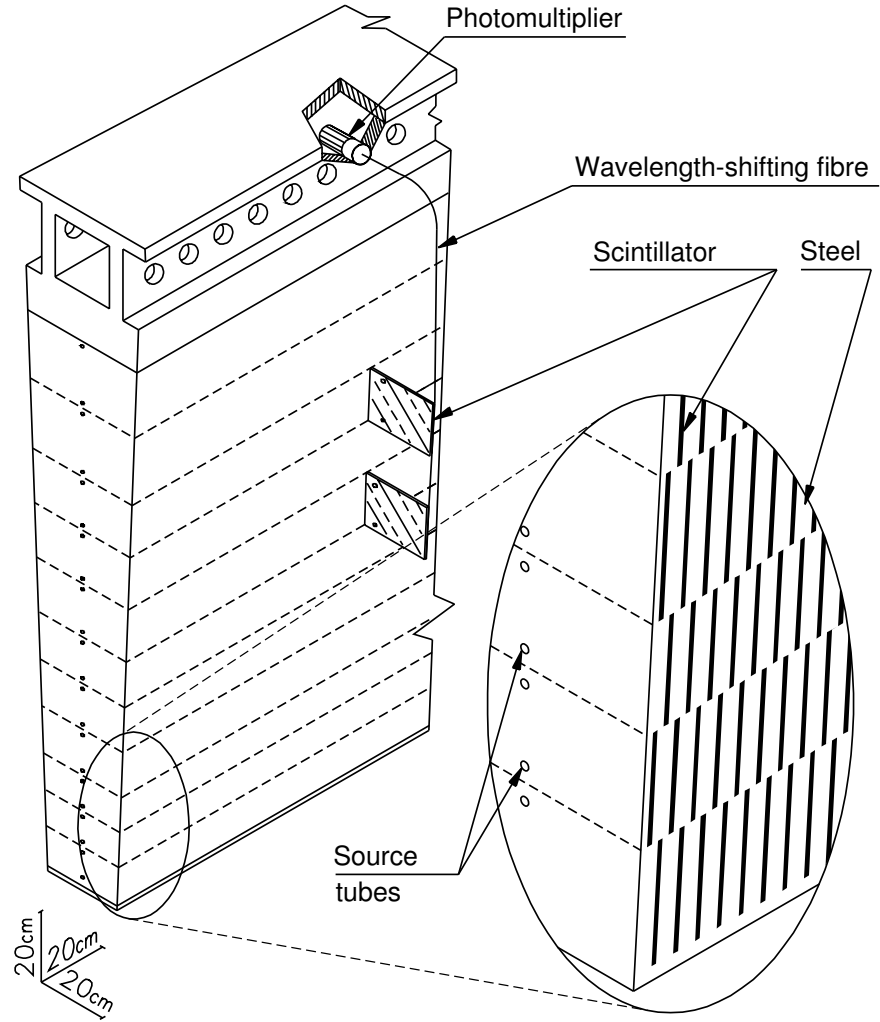


Figure 5.9: [3] Schematic of a tile calorimeter module including a depiction of the connection between the scintillator tile to the photomultiplier via a wavelength-shifting fibre.

689 EMC end-cap but sharing the same cryostat. This system uses copper as an absorber
 690 and liquid argon for the active material and covers the $1.5 < |\eta| < 3.2$ range using
 691 32 wdg-shaped modules per wheel. Finally, the FCal shares the same cryostat as the
 692 EMC and HEC end-caps and acts to extend the coverage of the combined calorimeter
 693 system to include the $3.1 < |\eta| < 4.9$ range. Each endcap contains 3 modules, the first
 694 an electromagnetic module (Copper/Liquid-Argon) which is followed by two hadronic
 695 modules which use (Tungsten/Liquid-Argon).

696 **5.4 Muon Spectrometer**

697 The ATLAS Muon Spectrometer (MS) [3], see figure 5.10, accomplishes tracking of
 698 charged particles in the $|\eta| < 2.7$ region for momentum reconstruction while also provid-
 699 ing triggering on charged particles in the $|\eta| < 2.4$ region. The magnetic field necessary
 700 for momentum reconstruction is provided by 3 air core torroid systems, one barrel tor-
 701 roid covering $|\eta| < 1.4$ and two endcap torroid systems which are inserted into the inner
 702 radius of the the barrel torroid to cover the $1.6 < |\eta| < 2.7$. The so called transition
 703 region $1.4 < |\eta| < 1.6$ between these two magnet systems is covered by a combination
 704 of the barrel and endcap torroid magnets. Similar to the ID the resolution is inversely
 705 proportional to the particle's incident momentum. Any muon with pT lower than 3GeV
 706 will never make it to the MS and thus will not be detected.

707 Precision tracking measurements for momentum reconstruction is accomplished using

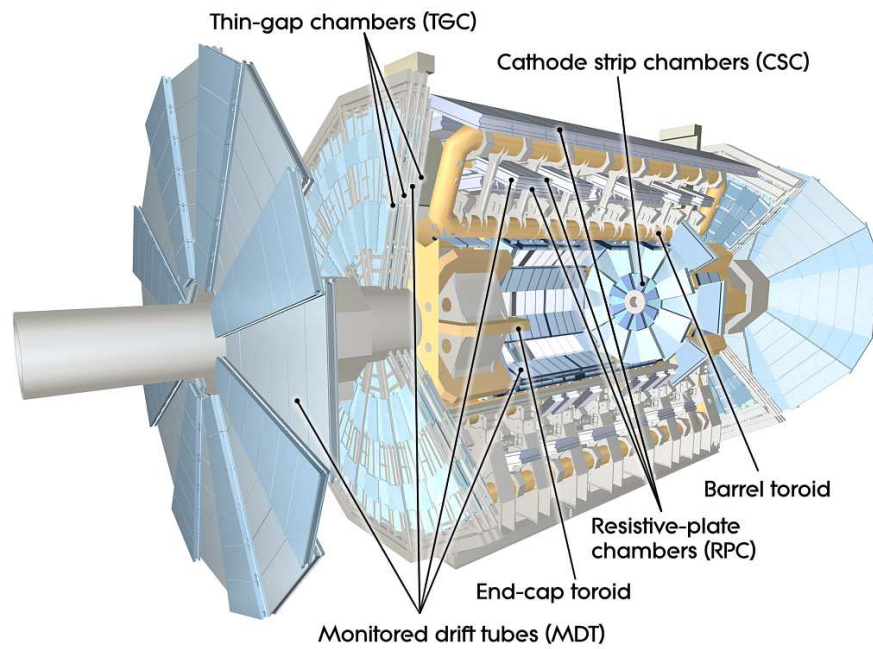


Figure 5.10: [3] A cut-away diagram of the ATLAS muon system and its many sub-detectors.

708 the Monitored Drift Tube chambers (MDTs) for $|\eta| < 2.0$ and using Cathode-Strip
709 Chambers (CSCs) for $2.0 < |\eta| < 2.7$. The MDT system consists of 1163 drift tube
710 chambers arranged in three to eight layers for varying η . The CSCs are designed to
711 withstand the higher rate and retain good time resolution using multiwire proportional
712 chambers with orthogonal segmented cathode planes.

713 The MS also gives nanosecond tracking information for triggering on muon tracks. This
714 is accomplished using Resistive Plate Chambers (RPC) in the barrel region $|\eta| < 1.05$
715 and Thin Gap Chambers (TGC) in the end-cap $1.05 < |\eta| < 2.4$ region. Both chamber
716 systems deliver a triggerable signal with a spread of 15–25 ns, thus providing the ability
717 to tag individual beam-crossings.

Part III

The HbbISR Analysis

720 Chapter 6

721 Data and Simulation Preparation

722 In order to compare data to theory ATLAS has developed an analysis chain which runs
723 both real data and simulated samples through the same processing, assuring a final
724 result which is as comparable as possible.

725 6.1 Data Used

726 6.2 Monte Carlo Samples

727 Chapter 7

728 Physics Object Selection

729 After the ATHENA Digitization step both data and monte carlo have the same format,
730 representing the three dimentional energy deposits. In order to analyze these deposits
731 they are cleaned, clustered and checked for overlap resulting in physics objects useful
732 for our specific analysis.

733 **7.1 Calorimeter Jets**

734 **7.2 Track Jets**

735 **7.3 Fat Jets**

736 **7.4 B-tagged Jets**

737 **7.5 Muons**

738 **7.6 Overlap Removal**

739 Chapter 8

740 Event Selection

741 Having created our physics objects we begin to make selections of what types of events
742 we want to consider given the goal of our analysis. In our boosted topology this means
743 considering things like momentum, jet collection efficiencies and background rejection.

744 8.1 Selected Triggers

745 8.2 Pre-selection Studies

746 8.3 Signal Selection

747 8.4 Optimisation

748 Chapter 9

749 Background Estimation

750 The dominant background was QCD. I worked on the $t\bar{t}$ control region. The V_{qq}
751 and single top backgrounds were estimated from monte carlo.

752 9.1 Multi-jet QCD estimation

753 9.2 $t\bar{t}$ control region

754 9.3 Single top estimation

755 9.4 Hadronic vector boson channel

756 **Chapter 10**

757 **Systematic Uncertainties**

758 **10.1 Theoretical Uncertainties**

759 **10.2 Experimental Uncertainties**

760 **Chapter 11**

761 **Statistical Fit**

762 The statistical fit in our analysis was accomplished using a framework developed for
763 Higgs searches.

764 **11.1 Profile Likelihood Function**

765 **11.2 Fit Configuration**

766 **11.3 Statistical Tests**

767 **Chapter 12**

768 **Results**

769 **12.1 Expectations**

770 **12.2 Statistical Analysis Results**

771 **12.3 Measurements and Limits**

772

Part IV

773

Conclusion

774 Chapter 13

775 Conclusion

776 I conclude that this section is the conclusion

Bibliography

- [1] Lyndon Evans and Philip Bryant. “LHC Machine”. In: *JINST* 3 (2008), S08001. DOI: 10.1088/1748-0221/3/08/S08001 (cit. on p. 24).
- [2] Chris Llewellyn Smith. “Genesis of the Large Hadron Collider”. In: *Phil. Trans. Roy. Soc. Lond.* A373.2032 (2014), p. 20140037. DOI: 10.1098/rsta.2014.0037 (cit. on p. 24).
- [3] ATLAS Collaboration. “The ATLAS Experiment at the CERN Large Hadron Collider”. In: *JINST* 3 (2008), S08003. DOI: 10.1088/1748-0221/3/08/S08003 (cit. on pp. 35, 37, 43–51).
- [4] Giordon Holtsberg Stark. “The search for supersymmetry in hadronic final states using boosted object reconstruction”. Presented 26 Apr 2018. May 2018. URL: <https://cds.cern.ch/record/2317296> (cit. on pp. 39, 40).
- [5] Karolos Potamianos. *The upgraded Pixel detector and the commissioning of the Inner Detector tracking of the ATLAS experiment for Run-2 at the Large Hadron Collider*. Tech. rep. ATL-PHYS-PROC-2016-104. 15 pages, EPS-HEP 2015 Proceed-

- 792 ings. Geneva: CERN, Aug. 2016. URL: <https://cds.cern.ch/record/2209070>
793 (cit. on p. 41).
- 794 [6] *ATLAS inner detector: Technical Design Report, 1*. Technical Design Report AT-
795 LAS. Geneva: CERN, 1997. URL: <http://cds.cern.ch/record/331063> (cit. on
796 p. 41).
- 797 [7] S Haywood et al. *ATLAS inner detector: Technical Design Report, 2*. Technical
798 Design Report ATLAS. Geneva: CERN, 1997. URL: [https://cds.cern.ch/](https://cds.cern.ch/record/331064)
799 [record/331064](https://cds.cern.ch/record/331064) (cit. on p. 41).
- 800 [8] B. Abbott et al. “Production and integration of the ATLAS Insertable B-Layer”.
801 In: *JINST* 13 (2018), T05008. DOI: 10.1088/1748-0221/13/05/T05008. arXiv:
802 1803.00844 [physics.ins-det] (cit. on p. 42).
- 803 [9] Christian Wolfgang Fabjan and F Gianotti. “Calorimetry for Particle Physics”.
804 In: *Rev. Mod. Phys.* 75.CERN-EP-2003-075 (Oct. 2003), 1243–1286. 96 p. DOI:
805 10.1103/RevModPhys.75.1243. URL: <https://cds.cern.ch/record/692252>
806 (cit. on p. 46).

807 **Appendix A**

808 **Hadronic Vqq Sherpa Studies**

809 Ancillary material should be put in appendices, which appear after the bibliography.